1 **Modeling of a compound flood induced by the levee breach at Qianbujing Creek,**

2 **Shanghai during Typhoon Fitow**

4 Yuhan Yang[1], Jie Yin[2, 3, 4*], Weiguo Zhang[1], Yan Zhang[2], Yi Lu[2], Yufan Liu[2], Aoyue Xiao[2],

5 Yunxiao Wang[2], Wenming Song[2]

7 1 State Key Laboratory of Estuarine and Coastal Research, East China Normal University, China

8 2 Key Laboratory of Geographic Information Science (Ministry of Education), East China Normal

9 University, China

10 3 Department of Civil and Environmental Engineering, Princeton University, USA

11 4 Institute of Eco-Chongming, East China Normal University, China

12 * Correspondence to: J.Y. (email: jyin@geo.ecnu.edu.cn)

14 *Competing interests*. The authors declare that they have no conflict of interest.

16 **Abstract:** Levee breach-induced flooding occurs occasionally but always causes considerable

17 losses. A serious flood event occurred due to the collapse of a 15-m-long levee section in

18 Qianbujing Creek, Shanghai, China, during typhoon Fitow in Oct 2013. Heavy rainfall

19 associated with the typhoon intensified the flood severity (extent and depth). This study

20 investigates the flood evolution to understand the dynamic nature of flooding and the compound

21 effect using a well-established 2D hydro-inundation model (Floodmap) to reconstruct this

22 typical event. This model coupled urban hydrological processes with flood inundation for high-

resolution flood modeling, which has been applied in a number of different environments, and Floodmap is now the mainstream numerical simulation model used for flood scenarios. Our simulation results provide a comprehensive view of the spatial patterns of the flood evolution. The worst-hit areas are predicted to be low-lying settlements and farmland. Temporal evaluations suggest that the most critical time for flooding prevention is in the early 1~3 hours after dike failure. In low-elevation areas, temporary drainage measures and flood defenses are equally important. The validation of the model demonstrates the reliability of the approach.

Key words: levee breach; compound flooding; inundation modeling; Shanghai

1. Introduction

Flooding is a common and devastating natural hazard, causing considerable personal injury, loss of life, and property damage worldwide (Jonkman et al., 2005; Jongman et al., 2012). Engineering measures such as dikes and barriers are typically constructed in low-lying deltas and floodplains to prevent flooding. However, weak or aging dikes without regular maintenance may fail during extreme flood events. Levee breaches may result in extensive flooding and damages throughout the hinterland (Ying et al., 2003). For example, Hurricane Katrina-induced flooding significantly damaged the dike system of New Orleans and overwhelmed the city, making it the costliest disaster in U.S. history (Kates et al., 2006). A more recent flood catastrophe with more than 50 deaths and hundreds of missing people resulted from a dam breach due to a Himalayan glacier outburst flood in northern India (Devjyot Ghoshal et.al, 2021).

In addition, the co-occurrence or subsequent occurrence of multiple flood drivers such as coastal high tide, storm surge, extreme precipitation, and high river flow resulting in large runoff may cause compound flooding. The compound effect is much greater than the effect of individual flood events (Wahl et al., 2015; Ghanbari et al. 2021). For instance, typhoon Fitow in 2013 brought torrential rain and caused high storm surges, resulting in record-breaking riverine water levels in the upstream region of the Huangpu River, Shanghai, China. As a result, the floodwall along the upstream Qianbujing Creek could not withstand the high water level, leading to a breach in a 15-m long section at 14:30 on 8 Oct 2013. Although the broken section

67 was repaired after about 8 hours, the levee breach combined with heavy precipitation resulted

68 in extensive flood inundation in the rural areas.

69

70 Over the last few decades, numerous studies analyzed the compound effects of various flood

71 hazards at different scales (Ganguli et al., 2020). Most previous studies focus on calculating the

72 joint flood risk probability. For instance, Lian et al (2013) evaluated the joint probability of

73 rainfall and tidal level both exceeding their threshold values through the copula and then

74 analyzed the combined effect of them on flood risk in a complex river network in a coastal city

75 in China. At a global scale, Couasnon (2020) and Eilander (2020) explored the compound flood

76 potential resulting from storm surges and riverine floods. Meanwhile, dike failure-induced

77 flooding and the compound effect have received increasing attention from decision-makers,

78 researchers, and even the general public. Recent studies have provided considerable progress

79 on dike reliability analysis and compound flood modeling (Curran et al., 2018; Naulin et al.,

80 2018). Several approaches for levee breach-induced flood modeling were developed. Some

81 previous studies have investigated the breaching mechanism and the hydrological process of

82 dike failure flooding, Vorogushyn (2010) proposed an Inundation Hazard Assessment Model

83 (IHAM), which coupled a 1D hydrodynamic model of river channel routing, a probabilistic

84 dike breach model, and a 2D raster-based inundation model. Cannata et al. (2011) used a GIS-

85 based approach to simplify a 2D dam break simulation. Recent advances have been made in the

86 application of methodologies for predicting the dike failure-induced flooding, Yin et al. (2020)

87 predicted dike failures and flood inundations in Shanghai, China, under various emission

88 scenarios using an interdisciplinary process-based approach.

89

90   The above studies contributed significantly to the modeling and evaluation of dike failure-

91   induced flooding, as well as compound flood risk. However, most previous studies have paid

92   attention to the occurrence probability and final impact of compound flooding. Few studies

93   investigated the complete compound dynamic hydrological process and mechanism of these

94   extreme cases. Moreover, few historical compound flooding events have been adequately

95   investigated in previous articles, these real-life cases play an important role to demonstrate the

96   feasibility and robustness of study results. To address the research gaps, this case study seeks

97   to examine the changing nature of levee breach-induced compound flooding. A 2D hydro-

98   inundation model Floodmap is used to simulate the process of the compound flood event that

99   occurred in Qianbujing Creek to improve our understanding of the evolution of flood

100   inundation. The results of the approach are validated by field measurements, including the

101   inundation depth and the flood extent over time. The findings can provide support for decision-

102   makers to develop flood adaptation measures.

103

104   **2.   Materials and methods**

105

106   **2.1 Study area**

107

108   The study area is located at the junction of the Huangpu River and Qianbujing Creek in the

109   upstream Huangpu River Basin, Shanghai, China. The rural area covers about 1.5 km^2 with the

110   majority being agricultural land and the minority being human settlements. It is characterized

by a mild and low-lying topography (with an average altitude of about 3 m above Wusong

Datum). Due to its location, the study area has faced high flood risk from the river system;

however, the heights of the flood defense measures are relatively low (i.e., a 50-year return

period flood protection standard) compared to the high floodwall (1000-year period flood

protection standard) along the middle and downstream urban regions of the Huangpu River

(Yin et al., 2020). Furthermore, because of the northern subtropical monsoon climate in this

region, pluvial flood events caused by extreme rainfall, typically associated with typhoons, are

frequently recorded during the flood season (June to September) (Yin & Zhang, 2015).

Therefore, the risk of compound flooding from both riverine and pluvial sources is significantly

higher than that in other locations. Figure 1 shows the location of the study area and the levee

breach during typhoon Fitow.

2.2 Data sources and processing

2.2.1   Topographic data

We use a high-resolution digital surface model (DSM) with the 6-m horizontal resolution, 0.1-

0.2m vertical resolution of the study area, which was constructed from images of the China

Resource 3 satellite (ZY-3) and other high-resolution satellites. Since buildings and trees

represent barriers to water flow and reduce the area available for water storage in the

hydrodynamic model, we remove the non-topographic features (e.g., trees and buildings)

according to the Google historical dataset of remote sensing images to generate a bare-earth

digital elevation model (DEM) based on the Wusong Datum of Shanghai. (Fewtrell et al., 2010; Neal et al., 2011; Yu & Lane, 2006b). We further resample the cell size of the bare-earth DEM from 6 m to 2 m using ArcGIS software to improve the spatial resolution of the flood inundation model. The simulation domain of the study area consisted of 0.3 million cells with an area of nearly 1.26 km^2.

2.2.2   Precipitation and water level

Time series of the precipitation and water level records during Typhoon Fitow is used as boundary conditions to simulate the hydrodynamic process of the levee breach-induced flooding and the rainfall-runoff. The data are typically derived from the stage measurements at gauge stations or radar-based rainfall data. However, due to the small scale of the study area, the gauging records are considered to be more reliable. Thus, we collected the historical records of the precipitation and water level data at the nearest gauging station from 0:00 on 8 Oct to 12:00 on 9 Oct 2013 for about 12 hours before and after the levee failure.

The station-based precipitation records (at one-hour intervals) are obtained from the Information Center of the Shanghai Meteorological Administration. The water level data (at 5 min intervals) at the closest gauging station along the Huangpu River (i.e. Songpu Bridge gauging station at the upstream of the Huangpu River, about 4 km away from Qianbujing Creek) are provided by the Shanghai Municipal Water Administration. The time series of the rainfall and water level data interpolated from the gauging stations is shown in Figure 2 (A, B). Heavy

rainfall occurred four hours before the levee breach, with the maximum hourly rainfall

exceeding 20 mm/h, resulting in the high water level of the river. Due to the high rainfall and

rising storm tide, the water level increased rapidly to nearly 4.8-m and caused the collapse of a

15-m long floodwall section at about 14:30 on 8 Oct.

2.2.3 Validation data

Aerial images or field surveys of flood extent are not available for the study event. There is also

a lack of water depth data from electronic gauges and flood incidents reported by the public.

Therefore, we validate the model through the field investigation of high watermarks in the study

area. We visited the study area three times in 2020 and investigated the residential areas (house

by house), roadways, and farmland mostly affected by the flood event. Validation data were

collected using questionnaires, and the coordinates of the locations were recorded by GPS.

However, since this flood event occurred more than 7 years ago, there are inherent uncertainties

in the investigation due to the changing environment and people's fading memory for the details

of the event. Similarly, people tend to exaggerate their injuries and losses during hazards; thus,

questionnaires can be highly biased. Finally, we pinpointed 32 incidents in total where locations

are confidently identified. Among the 32 observed inundation data, 14 were buildings, 10 were

roadways, and 8 were farmland locations (Figure 3).

2.3 Levee breach modeling

177 In general, levee breach mechanisms mainly include structural instability failures and structural

178 strength failures. The former pattern includes horizontal instability and rotational instability,

179 whereas the latter refers to the destruction of structures (Wang, 2016). Due to the configuration

180 of the floodwalls and the soil structure in Shanghai, structural instability failures always occur

181 during low water levels when critical inundation is less likely. In this case, structural strength

182 failure was considered the major reason for the levee breach in the study area, namely, the levee

183 collapse under an excessive hydraulic load on the wall due to an extremely high water level or

184 the uneven settlement of the floodwalls.

185

186 We identified the location of the levee breach from the historical news reports and through field

187 investigation. The 15-m long levee breach was located at the junction of Qianbujing creek and

188 the main channel of the Huangpu River. The levee height and location are obtained from the

189 Shanghai Municipal Institute of Surveying and Mapping. The height of the remaining intact

190 floodwalls without the breach section (about 5 m above Wusong Datum) is then overlaid onto

191 the original bare-earth DEM using the raster calculator in ArcGIS 10.6 software. Due to the

192 model cannot change the topography boundary during the running time, so we control the levee

193 height by changing the relative water level, namely before the levee breach, the relative water

194 level is 0 because there was no flooding, while during the levee breaching period, the relative

195 water level is the historical river water level, so that the flood spread from the breach section.

196

197 **2.4 Compound flood modeling**

198

199   The compound flood modeling is performed using a 2D hydro-inundation model (FloodMap)

200   (Yu & Coulthard, 2015; Yu & Lane, 2006a; 2006b), which couples hydrological processes (e.g.,

201   infiltration, evapotranspiration, and drainage) module with 2D surface flood inundation

202   modeling. The Floodmap model provides an effective approach for compound flood simulation,

203   allowing for more than one hydrological boundary condition, including pluvial, fluvial, coastal,

204   and groundwater sources. The fluvial flood modeling and pluvial flood modeling are described

205   in Sections 2.4.1 and 2.4.2, respectively.

206

207   **2.4.1   Fluvial flood modeling**

208

209   For simulating the levee breach-induced flooding, a simplified flood inundation module based

210   on a raster environment is used to solve the inertial form of the 2D shallow water equations.

211   The module considered the mass and momentum exchange between the river flow and

212   floodplain inundation, it has been used to simulate the dynamic nature of flood routing and to

213   extract potential flood maps (Yang et al., 2020; Yin et al., 2015). The 2D inundation model is

214   similar to the inertial algorithm of Bates et al. (2010). The difference is the time-step calculation

215   approach. The optimal time step is calculated using the subsequent iteration instead of using

216   the time step of the next iteration calculated by the current iteration. The main structure of the

217   model is presented below.

218

219   The Saint-Venant momentum equation without the convective acceleration has the following

220   form:

221 $$\frac{\partial q}{\partial t} + \frac{gh\partial(h+z)}{\partial x} + \frac{gn^2q^2}{R^{4/3}h} = 0 \tag{1}$$

222 where g is the acceleration of gravity, q is the flow per unit width, R is the hydraulic radius,

223 h is the water depth, z is the bed elevation, and n is Manning's roughness coefficient. For

224 wide and shallow flows, R can be approximated with h. The equation discretized with respect

225 to time is:

226 $$\frac{q_{t+\Delta t}-q_t}{\Delta t} + \frac{gh_t\partial(h+z)}{\partial x} + \frac{gn^2q_t^2}{h_t^{7/3}} = 0 \tag{2}$$

227 The q_t in the friction term can be replaced by $q_{t+\Delta t}$ to obtain the explicit expression in the

228 next time step:

229 $$q_{t+\Delta t} = \frac{q_t - gh_t\Delta t\left(\frac{\partial(h_t+z)}{\partial x}\right)}{\left(1+gh_t\Delta t n^2 q_t/h_t^{10/3}\right)} \tag{3}$$

230 The flows in the x- and y-directions are decoupled and have the same form. The discharge is

231 evaluated at the cell edges, and the depth is determined at the cell center. For model constancy

232 and minimizing numerical diffusion, we use the forward Courant-Friedrichs-Lewy condition

233 (FCFL), which was used by Yu & Lane (2011) for the diffusion-based version of FloodMap, to

234 calculate the time step in the inertial model:

235 $$\Delta t \leq \min\left(\frac{wd_id_jn}{d_i^{1.67}(S_i)^{1/2}+d_j^{1.67}(S_j)^{1/2}}\right) \tag{4}$$

236 where w represents the cell size, i and j are the indices for the flow direction in the x- and

237 y-directions, d_i and d_j are the effective water depths; S_i and S_j are the water surface

238 slopes. The effective water depth is defined as the difference between the high water surface

239 elevation and the high bed elevation of two cells that exchange water. The minimum time step

240 that satisfies the FCFL condition for all wet cells is used as the global time step for this iteration.

241 This approach does not require the back-calculation of the Courant number because the time

242 step is calculated based on the CFL condition that satisfies every wet grid cell for the current

243   iteration. The universal time step calculated with the FCFL may need to be scaled further by a

244   coefficient with a value between 0 and 1 because the FCFL condition is not strictly the right

245   stability criteria for an inertial system. A scaling factor in the range of 0.5–0.8 was found to

246   yield a stable solution in previous studies; here, a scaling factor of 0.7 is used for all simulations.

247   The calibration and validation of the model for the study area were conducted by Yin et al.

248   (2016).

249

250   **2.4.2   Pluvial flood modeling**

251

252   In terms of the pluvial flooding module, we run the surface water flood routing using the same

253   structure as the fluvial flooding module. The infiltration over saturation is calculated by the

254   widely used Green-Ampt equation, and the evapotranspiration is represented using a simple

255   seasonal sine curve of daily potential evapotranspiration (Calder et al., 1983). This module also

256   considered the amount of runoff loss to the urban storm sewer systems by scaling the drainage

257   capacity (mm/h) for each time step.

258

259   The infiltration over saturation is determined by the widely used Green–Ampt equation, which

260   approximates the rate of infiltration as a function of the capillary potential, porosity, hydraulic

261   conductivity, and time using the following form:

262     $$f(t) = K_s \left(\frac{\varphi_f + h_o}{z_f} + 1 \right) \tag{5}$$

263   where K_s expresses the hydraulic conductivity of the saturated soil, φ_f is the capillary

264   potential across the wetting front, h_o is the water ponding on the soil surface, and z_f is the

265   cumulative depth of infiltration.

266

267   The evapotranspiration is determined using a simple seasonal sine curve of daily potential

268   evapotranspiration (Calder et al., 1983) as follows:

269 $$E_p = \overline{E_p}\left[1 + \sin\left(\frac{360i}{365} - 90\right)\right] \tag{6}$$

270   where E_p is the mean daily potential evapotranspiration, and i is the day of the year. The

271   mass lost to evapotranspiration is typically limited due to the short duration of urban pluvial

272   flooding.

273

274   We use the topography boundary conditions, flow boundary conditions, and precipitation

275   boundary conditions as inputs to model a 36-h compound flood process, including the 12 h

276   before and after the levee breach, and we assumed evapotranspiration of 3 mm/day, a value that

277   which generates a good inundation prediction in the urbanized area (Yin et al., 2016; Yu and

278   Coulthard, 2015). The soil hydraulic conductivity (K_s) is an important but highly complex

279   parameter used to calculate infiltration. Empirically-based correlation methods or in situ

280   hydraulic laboratory measurements can be used to determine the value of K_s. Given the

281   practical constraints, this study refers to previous flood simulations in Shanghai (Yin et al.,

282   2016; Yin et al., 2015; Yu & Coulthard, 2015; Yu et al., 2016) and use the value of 0.001 m/h

283   for the hydraulic conductivity. A relatively high roughness value ($n = 0.06$) is used in the

284   simulation, according to the type of cultivated land and crops in the study area. Since the

285   Qianbujing creek is located in a rural area, we did not consider the urban storm drainage

286   capacity in this simulation.

287

3. Results and Discussion

289

3.1 Time series of flood inundation

291

Figure 4 shows the changes in the predicted flood inundation every 4 h during the event, and

Figure 2 (C, D) depicts the time series of average water depth and flood extent. These results

show the spatial and temporal evolution of the levee breach-induced compound flooding during

typhoon Fitow. Prior to the levee breach, it is apparent from Figures 4 and 5 that heavy rainfall

in the study area led to localized shallow waterlogging, mainly in the low-lying farmland and

forests. The inundation area reached its first peak in the early hours on 8 Oct, but the water

retention time was very short due to the shallow water depth (< 15 cm). At around 11:00 am on

8 Oct, another short-term rainstorm with rainfall over 20 mm/h occurred. Shortly after the

precipitation peak, the water level of Qianbujing Creek showed an increasing trend. The

compound effects of tide rising and heavy rain made the water level soon reached nearly 4.8 m

(Figure 2(A, B)). Due to the high water pressure, the bearing capacity of the floodwall was

exceeded, resulting in a 15-m breached section (at 14:30). Subsequently, overland flow through

breached floodwalls and extensive flood inundation occurred quickly along the riverbank, first

in the low-lying farmland near the river and then on roads and residential areas. About 10 homes

were completely inundated during the water level rising period (until 16:00) with the maximum

inundation depth higher than 2 m. After 16:00, as the rainfall stopped and the water level

dropped, the inundation area gradually stopped spreading.

309

A cross-comparison of the derived flood hazard maps over time further indicated that although

the rainstorm caused extensive surface water flooding in the majority of the study area, the

inundation depth was generally shallow (< 15 cm). This effect can be attributed to the

evapotranspiration and infiltration in a few hours. However, unlike the short-term waterlogging

caused by the rainstorm, the compound effects of the rainfall and levee breach-induced flood

inundation continued over 12 h, with an average water depth of nearly 60 cm.

316

3.2 Maximum flood inundation

318

The maximum flood extent and inundation during the event are shown in Figure 5. We use 2

cm as the threshold for surface water flooding and treat water depths shallower than 2 cm as

sheet flow, which did not accumulate in topographic lows (Yu et al., 2016). Figure 5 shows that

over half (56%) of the study area was inundated from the compound flooding, and most of the

flooded areas were low-lying farmland with maximum flood depths of higher than 2 m. Aside

from the waterfront areas, many low-lying farmland areas were affected by the rainstorm, with

maximum water depths over 50 cm. In contrast, the water depth on the roads and the buildings

were shallow; most of it was less than 0.5 m and disappeared quickly. In nearly half of the

flooded locations, the water depths were between 2 cm and 15 cm (44.1%), and a smaller

proportion of the area (21.12%) had water depths between 15 cm to 50 cm. About 33.26% of

the inundated areas had water depths of 50 cm to 2 m. In combination with the time series of

water level and rainfall (Figure 2 (A, B)), it can be inferred that the maximum flood inundation

331   occurred at about the fourth hour after the levee breaching (at ~16:00) in the waterfront area,

332   while it occurred at about 11:30 a.m. in other areas.

333

334   **3.3 Model validation**

335

336   The field measurements are used to validate the performance of the compound flooding model.

337   Figure 5 shows the location of the measurement points. The points are divided into building,

338   road, and farmland types. Since there are few residential areas in the study area, reliable

339   inundation information could not be obtained in most flooding areas. Therefore, most points

340   represent buildings with extensive inundation. Since there are uncertainties and errors in the

341   survey results, including the respondents' memory bias, exaggeration of inundation, and false

342   positives, we set the observed error to 5 cm for building points, 10 cm for road points, and 15

343   cm for farmland points. The simulation error is set as 5 cm. Figure 6 shows the scatter plot of

344   the simulated and observed water depth and the 95% confidence interval. A correlation is

345   observed between the simulated water depth and observed water depth, and most points fell

346   within the confidence band. The observed water depth was slightly higher than the simulated

347   water depth, which may be attributed to the exaggeration of the water depth by the respondents.

348

349   **3.4 Sensitivity analysis**

350

351   The model sensitivity to Manning's roughness coefficient over time is analyzed. Several

352   Manning's n values (0.01–0.1 at a 0.01 increment) are used for the roughness parameterization.

353 The difference between the average water depth (Figure 7A) and the total inundation area

354 (Figure 7B) predicted by the simulations with different n values is calculated on a cell-by-cell

355 basis. The results indicate similar trends of the average water depth and inundation area for

356 different roughness values and differences in the values. As the roughness increased, the

357 average water depth decreased, and the difference is more pronounced at higher roughness

358 values. For example, the maximum average depth decreased from 0.61 m to 0.55 m with an

359 increase in the n value of 0.01 to 0.1. Interestingly, there are differences in the sensitivity to the

360 roughness before and after the levee breach for the flood inundation extent. The inundation area

361 increases as the roughness rise during the rainstorm. However, the inundation area decreases

362 slightly with the growth of the n value during the levee breach when the river flow is the major

363 cause of the flooding. As a result, the rainfall is more likely to cause ponding with high

364 roughness, as it drops the flow velocity. Whereas, when the river flow is the main force, the

365 decline of roughness value leads to an increase in flood velocity which accelerates the spread

366 of flood. These results demonstrate the sensitivity of the model to the roughness.

367

368 **4. Conclusion**

369

370 Simulation of real-life historical severe flooding events can reveal the dynamic flooding process

371 and mechanism. In this study, a serious compound levee breach-induced flooding during the

372 typhoon Fitow has been adequately investigated used by a simple 2D hydro-inundation model

373 (Floodmap). The surface runoff caused by the rainstorm and river overflow is well considered

374 in the model.

375

The following conclusions can be drawn from the simulation results. Firstly, one key advantage of this modeling approach is the analysis of a single historic flood event. The flooding results showed the time series of the flooding extent and inundation depth, indicating that the low-lying area especially for farmland areas near the river had a very high flood risk. The compound flooding caused extensive damage to low-lying areas not only due to the elevation but the lack of a drainage network, resulting in an average water depth of over 0.5 m more than 12 h. Secondly, within 1-3 h after the dike failure, the floodwaters spread rapidly, and the inundation area and average water depth reached the peak value; chiefly because of the rising riverine tides at the same time, however, during the falling tide period, although the dike has not been repaired, the flooding diffusion tends to be slow, the flood risk decreased as the water level dropped as well. Thus, it can be indicated that the levee breach-induced flooding spread was heavily dependent on the change of riverine tides, the key period for levee breach-induced flooding control (such as repairing the levee, evacuation) was from levee breach to the end of the rising tide. Thirdly, the water does not drain rapidly only by infiltration or evaporation, and the waterlogging lasts for more than 12 h, resulting in the loss of farmland with high vulnerability. Therefore, for levee breach-induced flood response in the rural area, in addition to repairing the levee in time, it is essential to remove the flood water using drainage measures at the same time, such as setting water pumps near the farmland or other low-lying area. As well, the government should guide nearby residents to evacuate to a safe place when necessary.

Beyond the flood emergency response measures, effective long-term engineering measures may

397 be more suitable for fundamentally reducing the unpredictable levee-breach flooding risk.

398 Local specifications for flood-control engineering should be updated with the increasing flood

399 risk in the context of climate change (Yang et al., 2015).

400

401 Model validation is a challenging aspect of this research. The topographic data resolution, land

402 use, and land cover affect the simulation results. The validation data include field observations,

403 and the uncertainty is associated with incorrect recollections of the residents led to errors. It is

404 assumed that the error ranged from 5 cm to 15 cm for different land uses. Most of the

405 verification results match the field observations and fell within the confidence band,

406 demonstrating the model's reliability. Nevertheless, some of the simulated water depths are

407 slightly smaller than the field observations, which is attributed to the exaggeration of the depth

408 by the respondents.

409

410 Another important component of this study is the comparison of the predictions (flooding extent

411 and average water depth) using different Manning's n values (from 0.01 to 0.1 at a 0.01 interval).

412 The results demonstrated the model's sensitivity to roughness. Overall, the model exhibited

413 good reliability for single and compound flood modeling. Future researches on this topic may

414 focus on the following aspects to improve the robustness of the model. (1) Higher-resolution

415 topography and hydrological boundary conditions should be used to represent typical flood

416 conditions. (2) The drainage capacity could be modeled to provide a more reliable result. (3)

417 Urban compound flood risks should be evaluated to help decision-makers develop effective

418 emergency response plans and flood adaptation strategies.

419

Data Availability Statement. The raw and processed data from the co-authors' research findings cannot be shared at this time, as these data are also part of the ongoing research. The satellite remote sensing image came from the Google Earth open-source datasets (https://earth.google.com/);

424

Author contributions. YY and JY initiated and led this research. YY designed the flood event process, analyzed the performance of this model, and wrote the paper. JY provided history records of water level. WZ and JY gave the suggestion for this paper. YL dealt with the rainfall data. YZ, AX, YW and WS helped in collecting validation data.

Acknowledgments
This paper was supported by the National Natural Science Foundation of China (Grant no: 51761135024, 41871164), the National Key Research and Development Program of China (Grant no: 2017YFE0107400) and the Shanghai Sailing Program (Grant No. 21YF1456900).

Reference

Bates, P. D., Horritt, M. S., & Fewtrell, T. J. J. J. o. H. (2010). A simple inertial formulation of the shallow water equations for efficient two-dimensional flood inundation modelling. Journal of Hydrology, 387(1-2), 33-45.

Bevacqua, E., Maraun, D., Vousdoukas, M. I., Voukouvalas, E., & Widmann, M. J. S. A. (2019). Higher probability of compound flooding from precipitation and storm surge in Europe under anthropogenic climate change. Science Advances, 5(9), eaaw5531.

Calder, I. R., Harding, R. J., & Rosier, P. T. W. J. J. o. H. (1983). An objective assessment of soil-moisture deficit models. Journal of Hydrology, 60(1-4), 329-355.

Cannata, M., & Marzocchi, R. (2011). Two-dimensional dam break flooding simulation: a GIS-embedded approach. Natural Hazards, 61(3), 1143-1159.

Couasnon, A., Eilander, D., Muis, S., Veldkamp, T. I. E., Ward, P. J. J. N. H., & Sciences, E. S. (2020). Measuring compound flood potential from river discharge and storm surge extremes at the global scale. Natural Hazards and Earth System Sciences, 20(2), 489-504.

Curran, A., De Bruijn, K. M., & Kok, M. (2018). Influence of water level duration on dike breach triggering, focusing on system behaviour hazard analyses in lowland rivers. Georisk: Assessment and Management of Risk for Engineered Systems and Geohazards, 14(1), 26-40.

Devjyot Ghoshal., Manoj Kumar. (2021). Himalayan glacier breaks in India, around 125 missing in floods, https://www.reuters.com/article/us-india-disaster-idUSKBN2A706O

Eilander, D., Couasnon, A., Ikeuchi, H., Muis, S., Yamazaki, D., Winsemius, H. C., & Ward, P. J. J. E. R. L. (2020). The effect of surge on riverine flood hazard and impact in deltas globally. Environmental Research Letters, 15(10), 104007 (104012pp).

Fewtrell, T. J., Bates, P. D., Horritt, M., & Hunter, N. M. J. H. P. (2010). Evaluating the effect of scale in flood inundation modelling in urban environments. Hydrological Processes, 22(26), 5107-5118.

Ganguli, P., Paprotny, D., Hasan, M., Güntner, A., & Merz, B. (2020). Projected Changes in Compound Flood Hazard From Riverine and Coastal Floods in Northwestern Europe.

461   Earth's Future, 8(11). doi:10.1029/2020ef001752

462   Ghanbari, Mahshid et al. 2021. "Climate Change and Changes in Compound Coastal-Riverine
463   Flooding Hazard Along the U.S. Coasts." Earth's Future 9(5).
464   http://tidesandcurrents.noaa.gov/ (September 28, 2021).

465   Jongman, B., Ward, P. J., & Aerts, J. C. J. H. (2012). Global exposure to river and coastal
466   flooding: Long term trends and changes. Global Environmental Change, 22(4), 823-835.
467   doi:10.1016/j.gloenvcha.2012.07.004

468   Jonkman, S. N. (2005). Global perspectives of loss of human life caused by floods. Natural
469   Hazards, 34(2), 151-175.

470   Lian, J. J., Xu, K., Hydrology, C. M. J., Sciences, E. S., & Discussions. (2013). Joint impact of
471   rainfall and tidal level on flood risk in a coastal city with a complex river network: a case
472   study of Fuzhou City, China. Hydrology and Earth System Sciences, 17(1), 679-689.

473   Moftakhari, H. R., Salvadori, G., AghaKouchak, A., Sanders, B. F., & Matthew, R. A. (2017).
474   Compounding effects of sea level rise and fluvial flooding. Proceedings of the National
475   Academy of the Sciences of the United States of America, 114, 9785-9790.

476   Naulin, M., Kortenhaus, A., & Oumeraci, H. (2018). Reliability-Based Flood Defense Analysis
477   in an Integrated Risk Assessment. Coastal Engineering Journal, 57(1), 1540005-1540001-
478   1540005-1540035.

479   Neal, J., Schumann, G., Fewtrell, T., Budimir, M., Bates, P., & Mason, D. J. J. o. F. R. M.
480   (2011). Evaluating a new LISFLOOD-FP formulation with data from the summer 2007
481   floods in Tewkesbury, UK. Journal of Flood Risk Management, 4(2).

482   Vorogushyn, S., Merz, B., Lindenschmidt, K. E., & Apel, H. (2010). A new methodology for
483   flood hazard assessment considering dike breaches. Water Resources Research, 46(8).
484   doi:10.1029/2009wr008475

485   Wahl, T., Jain, S., Bender, J., Meyers, S. D., & Luther, M. E. (2015). Increasing risk of
486   compound flooding from storm surge and rainfall for major US cities. Nature Climate
487   Change, 5(12), 1093-1097.

488   Yang, L., Scheffran, J., Qin, H. et al. (2015) Climate-related flood risks and urban responses in
489   the Pearl River Delta, China. Regional Environmental Change, 15, 379–391.
490   https://doi.org/10.1007/s10113-014-0651-7

491   Yang, Y., Yin, J., Ye, M., She, D., & Yu, J. (2020). Multi-coverage optimal location model for
492   emergency medical service (EMS) facilities under various disaster scenarios: a case study
493   of urban fluvial floods in the Minhang district of Shanghai, China. Natural Hazards and
494   Earth System Sciences, 20(1), 181-195.

495   Yin, J., Jonkman, S., Lin, N., Yu, D., & Wang, J. J. E. s. F. (2020). Flood Risks in Sinking
496   Delta Cities: Time for a Reevaluation? Earth's Future, 8(8).

497   Yin, J., Yu, D., & Wilby, R. (2016). Modelling the impact of land subsidence on urban pluvial
498   flooding: A case study of downtown Shanghai, China. Science of the Total Environment,
499   544(July 2011), 744-753.

500   Yin, J., Yu, D., Yin, Z., Wang, J., Xu, S. J. L., & Planning, U. (2015). Modelling the
501   anthropogenic impacts on fluvial flood risks in a coastal mega-city: A scenario-based case
502   study in Shanghai, China. Landscape and Urban Planning, 136, 144-155.

503   Yin, J., & Zhang, Q. (2015). A comparison of statistical methods for benchmarking the
504   threshold of daily precipitation extremes in the Shanghai metropolitan area during 1981–

2010. Theoretical and Applied Climatology, 120(3-4), 601-607.

Ying, X., Wang, S. S. Y., & Khan, A. A. (2003). Numerical Simulation of Flood Inundation due to Dam and Levee Breach. Paper presented at the World Water & Environmental Resources Congress.

Yu, D., & Coulthard, T. J. J. J. o. H. (2015). Evaluating the importance of catchment hydrological parameters for urban surface water flood modelling using a simple hydro-inundation model. Journal of Hydrology, 524, 385-400.

Yu, D., & Lane, S. N. (2006a). Urban fluvial flood modelling using a two-dimensional diffusion-wave treatment, part 1: Mesh resolution effects. Hydrological Processes, 20(7), 1541-1565.

Yu, D., & Lane, S. N. (2006b). Urban fluvial flood modelling using a two-dimensional diffusion-wave treatment, part 2: Development of a sub-grid-scale treatment. Hydrological Processes, 20(7), 1567-1583.

Yu, D., & Lane, S. N. (2011). Interactions between subgrid-scale resolution, feature representation and grid-scale resolution in flood inundation modelling. Hydrological Processes, 25(1), 36-53.

Yu, D., Yin, J., & Liu, M. (2016). Validating city-scale surface water flood modelling using crowd-sourced data. Environmental Research Letters, 11(12).
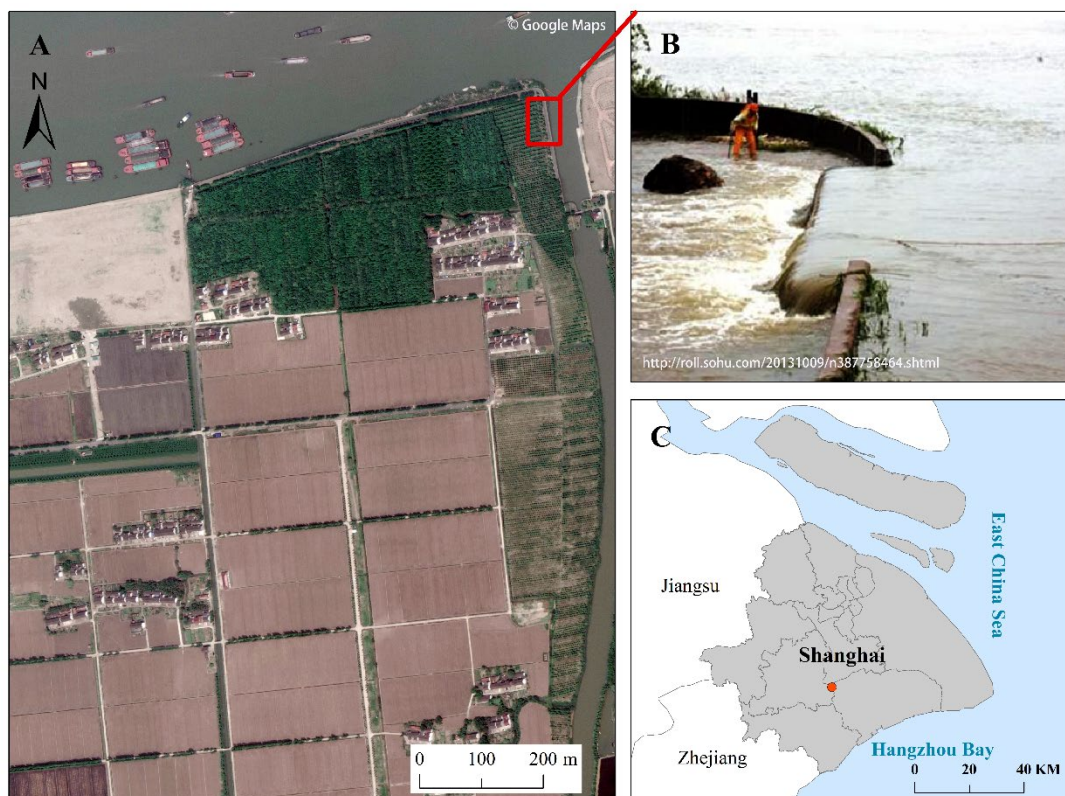
Fig. 1 Location of the study area and levee breach during typhoon Fitow
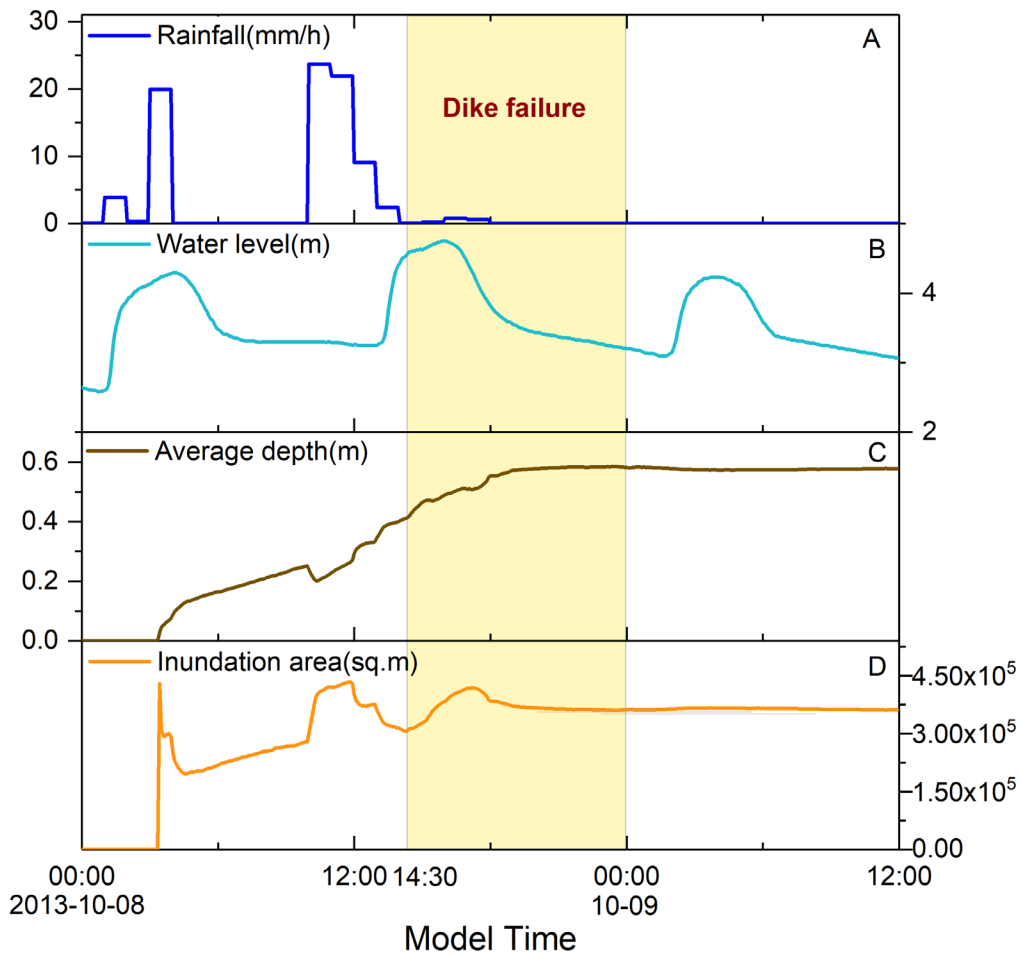
526

527   Fig.2 Time series of the rainfall(A) and water level(B) data at Qianbujing Creek during

528   Typhoon Fitow; Time series of simulated average water depth(C) and inundation area(D)

529

530

531

532   Fig. 3 Field investigation of flood inundation after the event
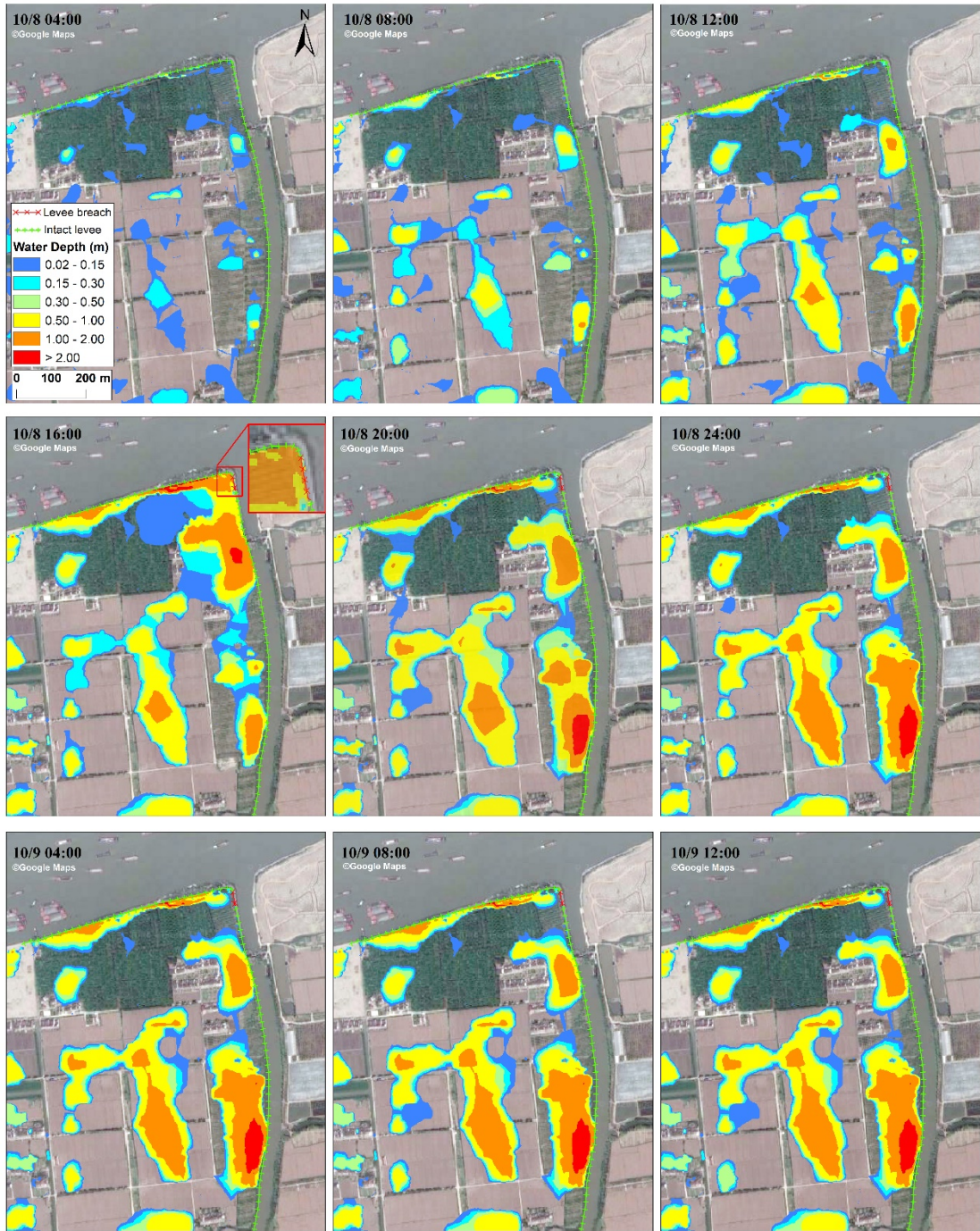
533

534   Fig. 4 Time series of flood inundation during the typhoon event

535
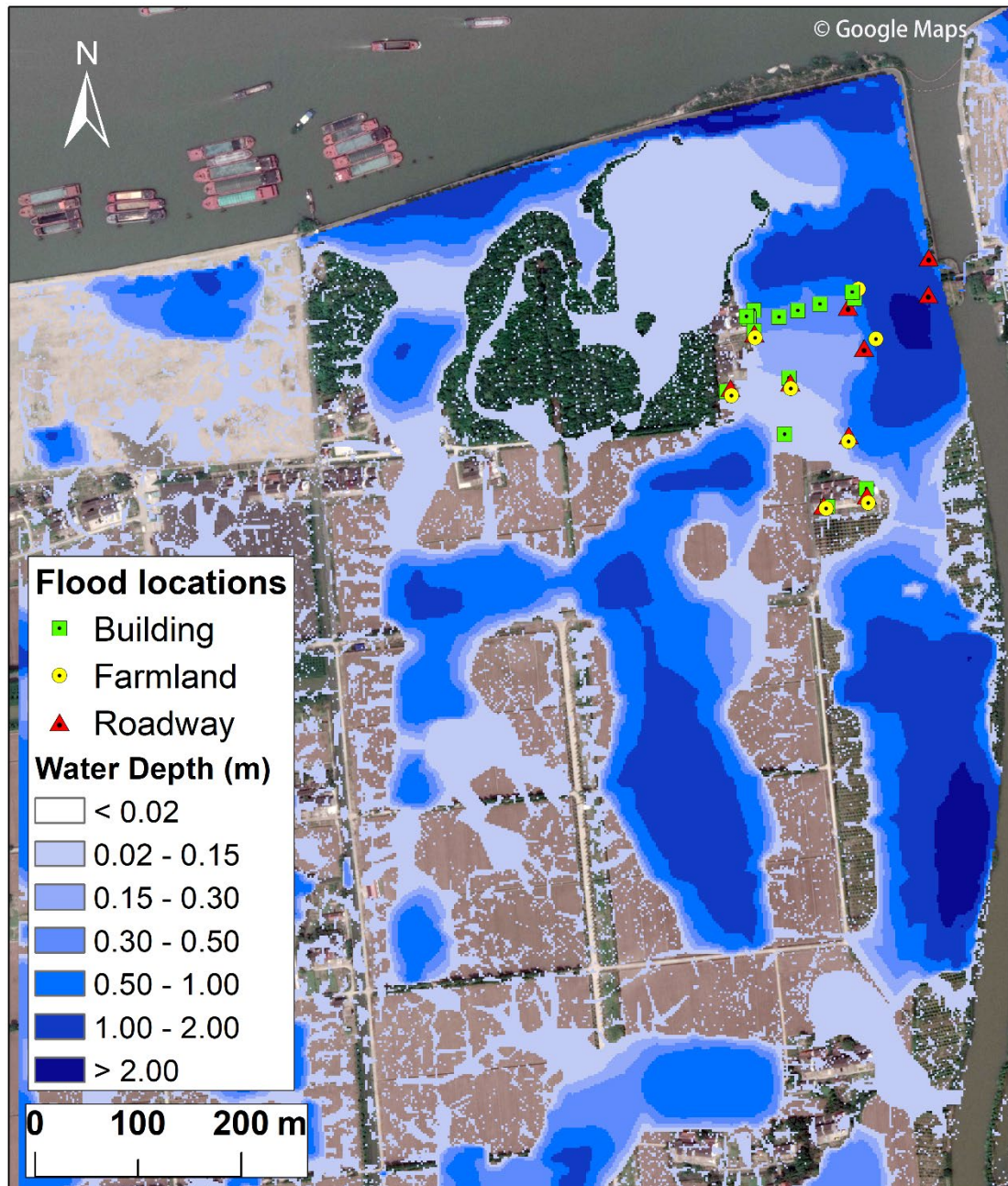
536

537   Fig. 5 Maximum flood extent and depth predicted by the model
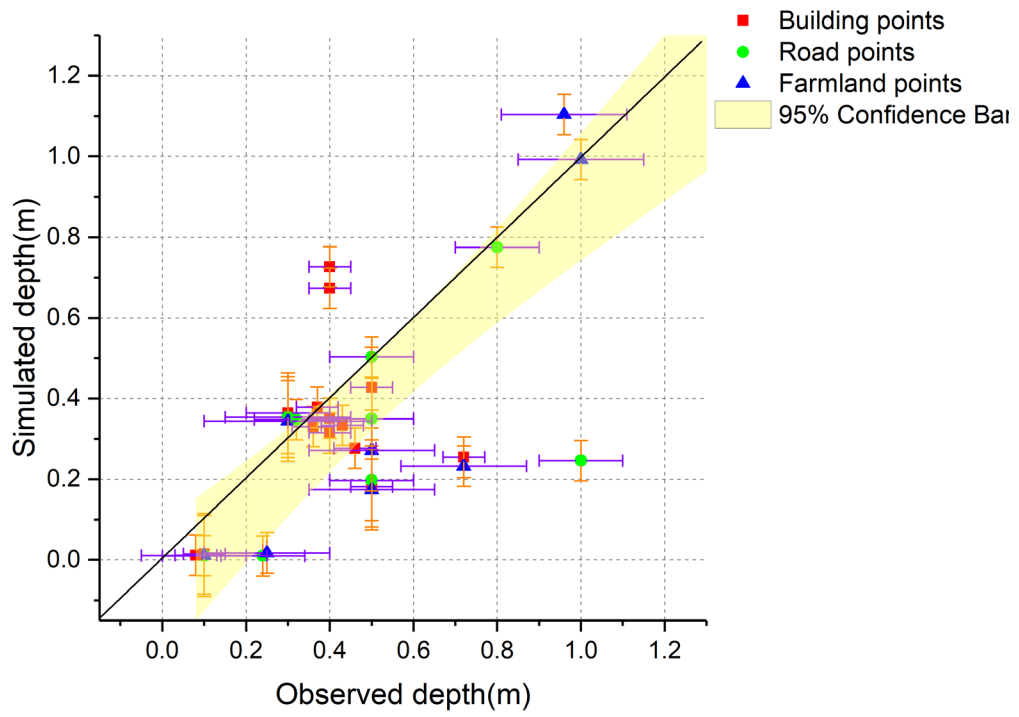
538

539      Fig. 6 A comparison of the simulated and observed depths

540

541
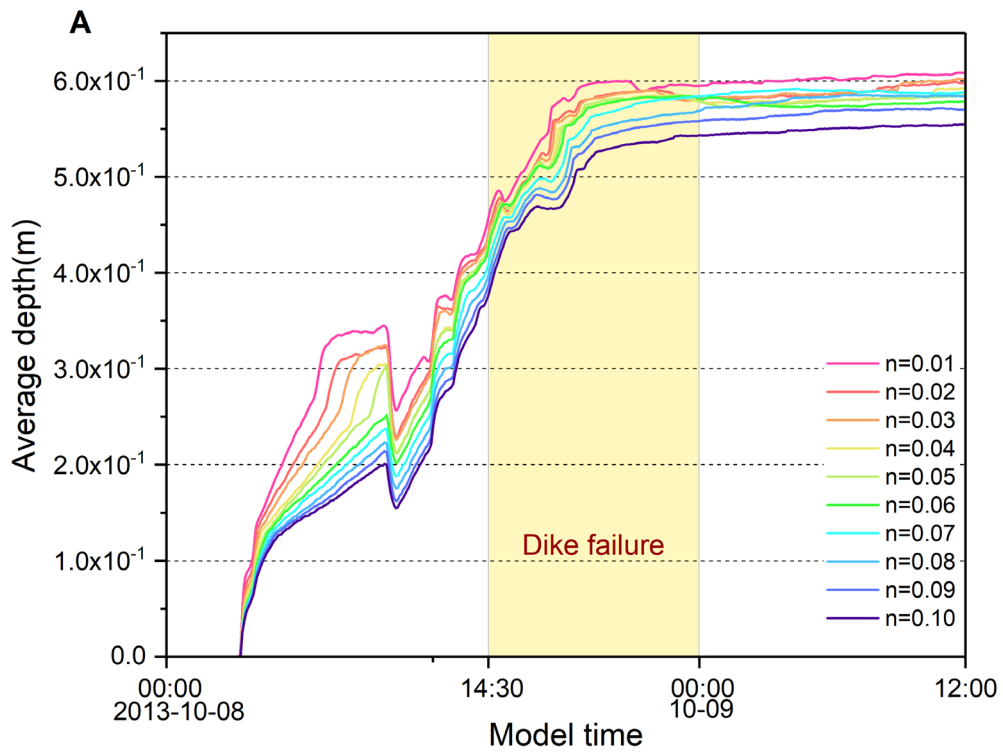
542
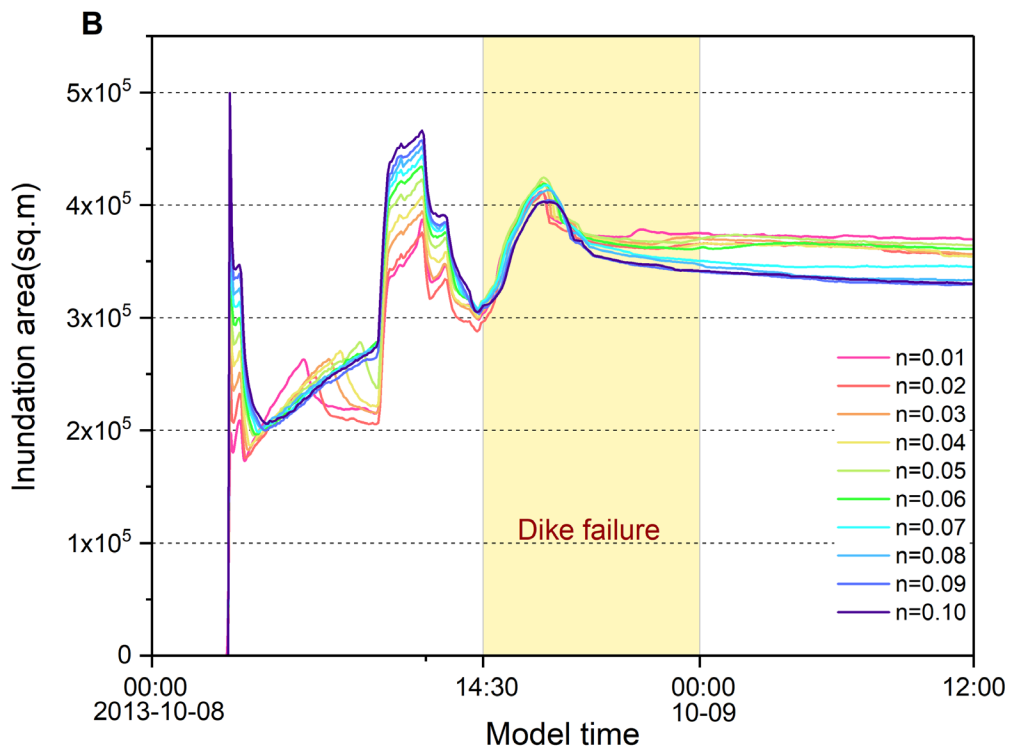
543

544   Fig. 7 Sensitivity analysis of the model to Manning's roughness coefficient